Self-assembled microactuators using chiral liquid crystal elastomers

*Yoo Jin Lee, Mustafa K. Abdelrahman, Manivannan Sivaperuman Kalairaj, and Taylor H. Ware**

Yoo Jin Lee, Manivannan Sivaperuman Kalairaj, Prof. Taylor H. Ware
Department of Biomedical Engineering
Texas A&M University
College Station, TX 77843, United States
E-mail: taylor.ware@tamu.edu

Mustafa K. Abdelrahman, Prof. Taylor H. Ware
Department of Materials Science and Engineering
Texas A&M University
College Station, TX 77843, United States

Keywords: actuators, microarrays, liquid crystal elastomers, self-assembly, stimuli-responsive polymers

Abstract

Materials that undergo reversible changes in form typically require top-down processing to program the microstructure of the material. As a result, it is difficult to program microscale, 3D shape morphing materials that undergo non-uniaxial deformations. Here, we describe a simple bottom-up fabrication approach to prepare bending microactuators. Spontaneous self-assembly of liquid crystal monomers with controlled chirality within 3D micromold results in a change in molecular orientation across thickness of the microstructure. As a result, heating induces bending in these microactuators. We vary the concentration of chiral dopant to adjust the chirality of the monomer mixture. LCE microactuators doped with 0.05 wt% of chiral dopant produce needle-shaped actuators that bend from flat to an angle of 27.2 ± 11.3 ° at 180 °C. Higher concentrations of chiral dopant lead to actuators with reduced bending, and lower concentrations of chiral dopant lead to actuators with poorly controlled bending. Asymmetric molecular alignment inside 3D structure is confirmed by sectioning actuators. Arrays of microactuators that all bend in the same direction can be fabricated if symmetry of

geometry of the microstructure is broken. We envision our new platform to synthesize microstructures can further be applied in soft robotics and biomedical devices.

1. Introduction

Developing microscale, 3D shape morphing structures presents a complex challenge. While machines equipped with batteries, sensors, processors, and motors can be designed to perform programmed shape change in response to stimulus,[1] it is difficult to scale down the system to a microscale due to the functional components. To achieve such responsive, programmed shape change at the microscale, stimuli-responsive polymers offer substantial advantages. Stimuli-responsive polymers undergo significant changes in properties in response to environmental changes.[2] The inherent ability of stimuli-responsive polymers to function as both sensors and actuators offers advantages in the fabrication of microscale actuators.[3,4] However, developing effective processing strategies for programming the microstructure of the materials still remains challenging.

Programmable shape morphing of microstructures requires processing strategies to pattern the magnitude or anisotropy of deformation. Stimuli-responsive polymers can be fabricated into shape morphing microstructures by top-down or bottom-up approaches. Top-down approaches create microstructures from bulk materials.[5,6] In top-down approaches, programmable shape morphing can be realized by inducing heterogeneity, such as in crosslink density, within a material through the variation of processing conditions.[7–9] Although top-down approaches offer high precision and controllability, fabrication throughput scales directly with resolution.[10,11] Bottom-up approaches can create shape morphing structures by assembling units at the molecular level into a larger object.[12,13] Directing this self-assembly is an important component of fabricating a structure with the desired response.[14,15]

Liquid Crystal Elastomers (LCEs) have been considered promising stimuli-responsive polymers for realizing shape morphing microstructures. LCEs are lightly crosslinked polymer networks comprised of mesogenic monomers that typically exhibit a nematic phase.[16,17] These soft materials undergo large, reversible shape changes in response to an external stimulus.[18] The shape morphing behavior of LCEs arises from the reversible order-disorder transition of the material and resulting changes in the conformation of polymer chains.[18–20]

Simple expansion or contraction of LCE microactuators can be achieved by uniaxial compression where the applied compression forces bring the reorientation of mesogens.[21–23] More complex shape changes can be obtained by using magnetic fields, which generate uniform director fields within LCEs that can be aligned at arbitrary angles.[24] Starting with the work of Keller group to create LCE microactuators,[25] LCE microactuators that can undergo various shape changes, such as shrinking, bending, and twisting, have been developed.[26–28] However, it is challenging to apply a spatially-complex magnetic field across a small sample thus somewhat limiting the types of shape transformations that can be achieved. Microfluidic devices can also be used to create microsized LCE particles. In this method, droplets of liquid crystal monomers are generated by injecting them into the stream of an immiscible fluid. The liquid crystal monomers confined in droplets self-assemble, and the alignment gets subsequently locked in via crosslinking.[29–31] Although this approach enables the mass production of microsized LCEs, it has limitations in producing LCEs with different forms.

In this work, we introduce new tools to develop 3D LCE microactuators that bend on heating. We take advantage of the spontaneous self-assembly of chiral nematic monomer solutions within microsized molds (**Figure 1**a). When doped with an optimized amount of chiral dopant, molecules self-assemble asymmetrically across the thickness of the microactuator, which results in thermally responsive, reversible, and large bending deformation of the microactuator (Figure 1b, c). In addition to chirality, protrusions were introduced onto LCEs to control the molecular orientation and control the direction of bending. Our fabrication strategy programs bending of microactuators in both magnitude and direction without complex setups and allows for scaling up to arrays of actuators.

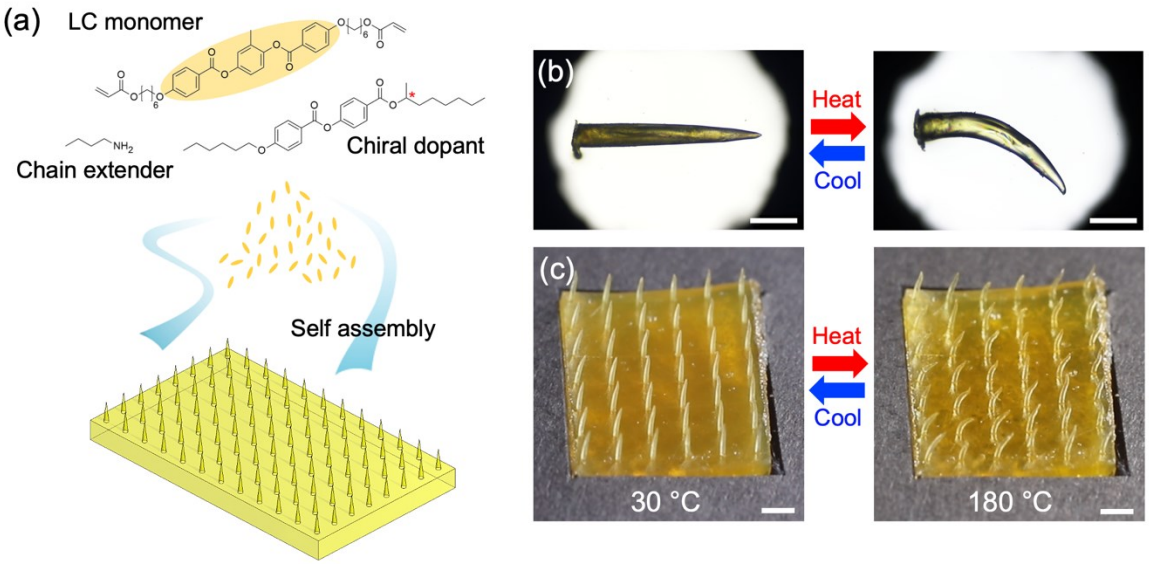

Figure 1. a) Schematic depicting the spontaneous self-assembly of liquid crystal mixture within microsized cavities to produce arrays of LCE microactuators. b) Images showing the bending deformation of a single LCE microactuator and c) LCE microactuator arrays in response to temperature. Scale bar, 500 μm (b) and 2 mm (c).

2. Results and Discussion

2.1. Fabrication of LCE microactuators

LCE microactuators were fabricated by casting a liquid crystal (LC) monomer mixture onto a PDMS mold of microneedles (**Figure 2**a). LCE microactuators were shaped as microneedles because the size and shape can be advantageous in a wide range of applications, from microgrippers[32,33] to microbots.[34,35] Under vacuum, LC mixture composed of reactive LC monomer (RM82), chain extender (n-butylamine), photoinitiator (I-369), and chiral dopant (R811) was filled into microscale cavities of PDMS mold in nematic state. LC monomers in the nematic phase spontaneously self-assemble into ordered domains and undergo chain extension by aza-Michael addition reaction, yielding LC oligomers.[36] The oligomers were crosslinked into elastomers by photopolymerization, which locks in molecular orientation within the microstructures.

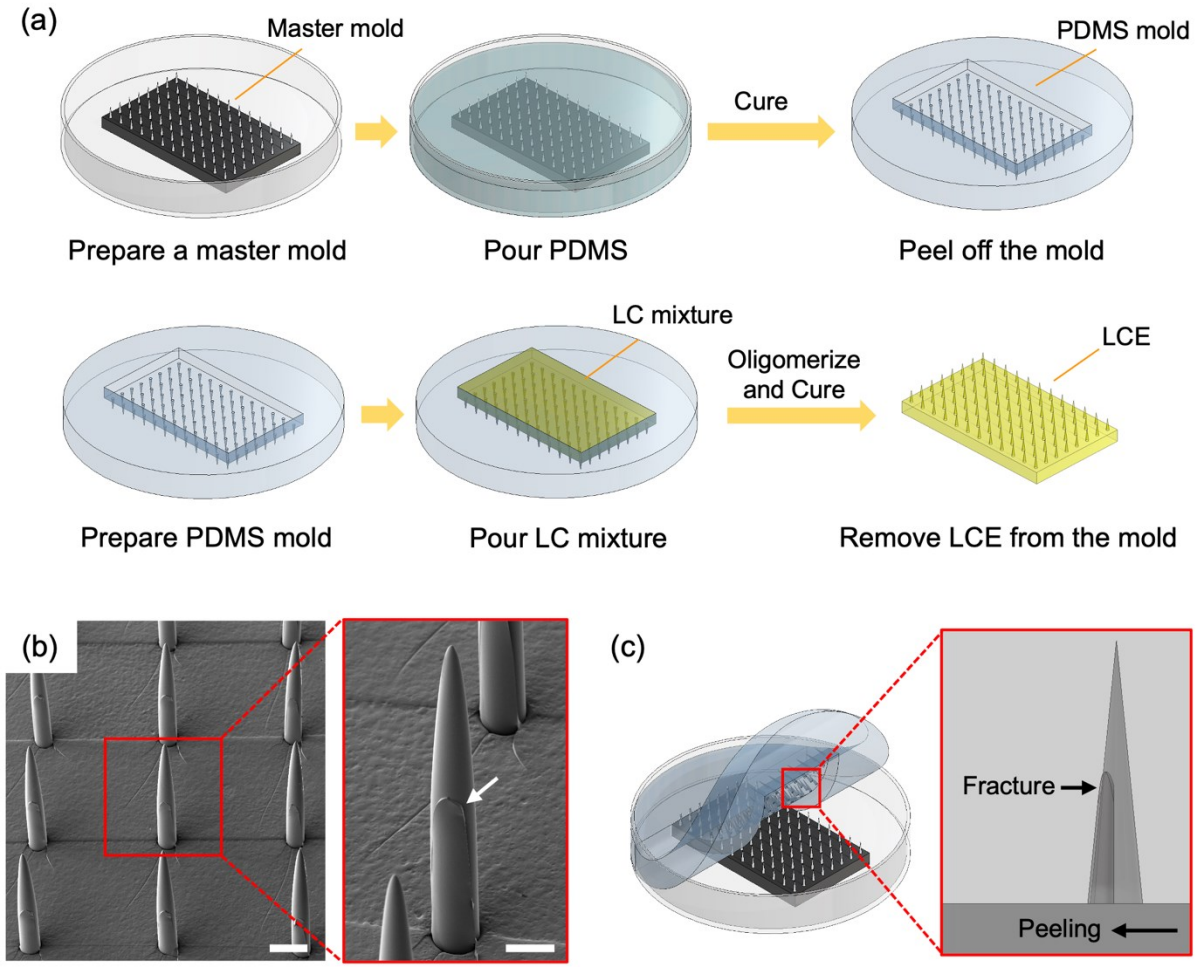

Figure 2. Fabrication and characterization of LCE microactuator arrays. a) Schematic of the fabrication process of PDMS mold and LCE microactuator arrays. b) Representative scanning electron microscopy (SEM) images of LCE microactuator arrays demonstrating the uniformity in shape and position of protrusion. In the magnified view of a single microactuator, the white arrow indicates the protrusion. Scale bar, 500 µm (left) and 250 µm (right). c) Illustration showing the formation of fracture on PDMS mold during peeling process. The arrows indicate peeling direction and corresponding fracture position.

2.2. Surface morphology of LCE microactuators

Surface morphology and dimensions of synthesized LCE microactuator arrays were analyzed (Figure 2b and Figure S1). The arrays consisted of 2 mm tall microactuators in a tapered conical shape with a base diameter of 278.2 ± 13.5 µm (n=9). Each LCE has a uniform protrusion (n=9). When peeling PDMS from master mold, high aspect ratio of microneedles of the master mold causes the PDMS to crack.[37,38] The crack propagates in a trailing meniscus shape, releasing elastic strain energy stored in PDMS[39, 40] and ultimately producing fracture on PDMS (Figure 2c).[41] During the fabrication of microactuators, the fracture on PDMS gets transferred onto LCE microactuators, yielding a protrusion on the actuators. The dimensions of protrusion were a height of 757.6 ± 73.0 µm and a base width of 231.6 ± 53.1

μm (n=5). The consistency in the position of protrusion on LCE microactuators was confirmed by SEM (Figure 2b).

2.3. Bending of LCE microactuators driven by chirality

Chiral liquid crystal monomer solutions within microsized mold self-assemble in an asymmetric manner, leading to a shape change of bending in response to temperature. LCE microactuators with varying concentrations of chiral dopant were prepared, and thermo-responsive behavior was analyzed (**Figure 3**a, b, see Figure S2 for the definition of bending angle). When heated from 30 to 180 °C, all LCE microactuators showed bending behavior (Figure 3a, Movie S1). Upon cooling to 30 °C, LCE microactuators return to the initial straight shape. The bending behaviors suggest that the self-assembly of chiral liquid crystal monomers within microsized mold generates an asymmetric molecular orientation across the thickness of LCE microactuators.

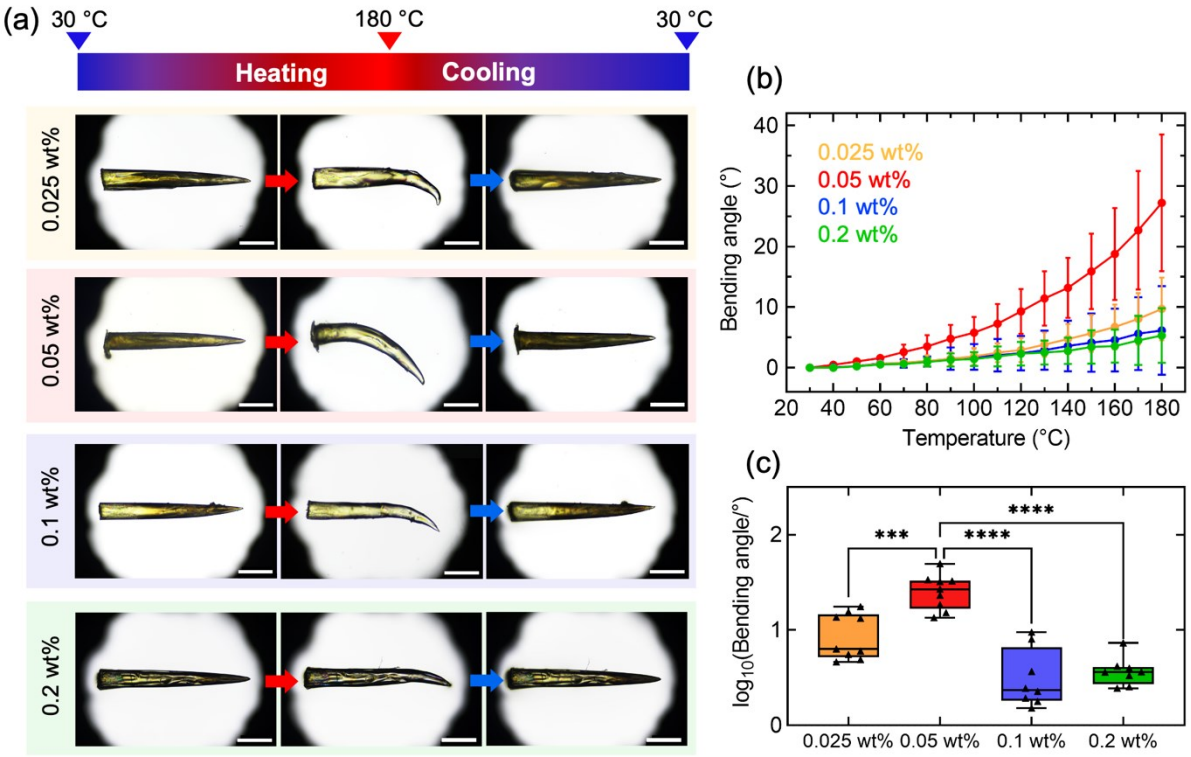

Figure 3. Controlling bending angle by adjusting chiral dopant concentration. a) Representative images showing reversible bending actuation of single LCE microactuator in response to temperature. The four rows show thermo-responsive behaviors in LCEs with different concentrations of chiral dopant. The images were acquired using brightfield unpolarized microscopy. Scale bar, 500 μm. b) Bending angle of the LCE microactuator as a function of temperature at varying chiral dopant concentrations. Bending angles were measured from the second heating cycle. Each data point represents a mean, and error bars represent a standard deviation (n=9 independent samples for each group). c) Box-and-whisker plot analyses of log-transformed bending angles at 180 °C at different chiral dopant

concentrations (n=9, 9, 8, and 8 independent samples from left to right; *** p<0.001; **** p<0.0001).

The bending behavior of LCE microactuators is strongly influenced by the concentration of chiral dopant. When no chiral dopant was introduced, LCE microactuators showed unpredictable bending angle and direction (Figure S3). A more controlled bending deformation was achieved by adding chiral dopant (0.025, 0.05, 0.1, and 0.2 wt%), and the concentration of chiral dopant affected the magnitude of bending in LCE microactuators. As shown in Figure 3a and b, the bending angle of LCE microactuators increased with the increase of the chiral dopant concentration from 0.025 to 0.05 wt%. Beyond that point, a further increase in dopant concentration results in a decrease in bending angle of LCEs. The decrease in bending angle, when dopant concentration exceeds 0.05 wt%, can be related to pitch of the monomer mixture in relation to size of LCE microactuator. Considering helical twisting power (*HTP*) of chiral dopant R811 ($HTP \approx 11\ \mu m^{-1}$),[42,43] pitch is approximately 182 μm at 0.05 wt% of dopant concentration. With the increase of dopant concentration from 0.05 wt% to 0.2 wt%, pitch decreases from 182 to 45 μm. As pitch becomes considerably smaller than the diameter of actuator, the director twists multiple times within the actuator. This twisting results in a more symmetric molecular structure and decreased bending deformation.

LCEs with 0.05 wt% of chiral dopant exhibited the maximum bending angle of 27.2 ± 11.3 ° at 180 °C. To determine whether the bending angle of LCEs with 0.05 wt% of chiral dopant is significantly larger than other groups, results were statistically analyzed using ordinary one-way ANOVA followed by Dunnett's multiple comparisons test. Since data follow a heavy-tailed distribution, we took the logarithm of raw values of bending angles. The bending angle of LCEs with 0.05 wt% of chiral dopant was significantly larger than LCEs with 0.025, 0.1, and 0.2 wt% of chiral dopant (p<0.001, p<0.0001, and p<0.0001, respectively) (Figure 3c). LCEs with 0.05 wt% of chiral dopant demonstrated repeatable bending performance over 10 thermal cycles between 30 and 180 °C (Figure S4).

In LCEs with 0.05 wt% of chiral dopant, a slight deflection near tip was occasionally observed in addition to the significant curvature in the middle of actuators (Figure S5). The deflection near the tip occurred in various directions. The inefficiency of chiral dopant in

controlling deflection near the tip is probably because factors other than chirality, such as surface energy, become increasingly influential in determining the molecular alignment as the dimension of the mold decreases to micron size.[44]

2.4. Molecular orientation inside LCE microactuators

The bending deformation originates from the molecular alignment within LCE microactuators. Understanding the molecular orientation of thick LCEs with complex director orientation requires samples to be cut into thinner sections. Here, LCE microactuators were sectioned in directions perpendicular to the long axes, and the molecular alignment across cross-sections was assessed (**Figure 4**a).

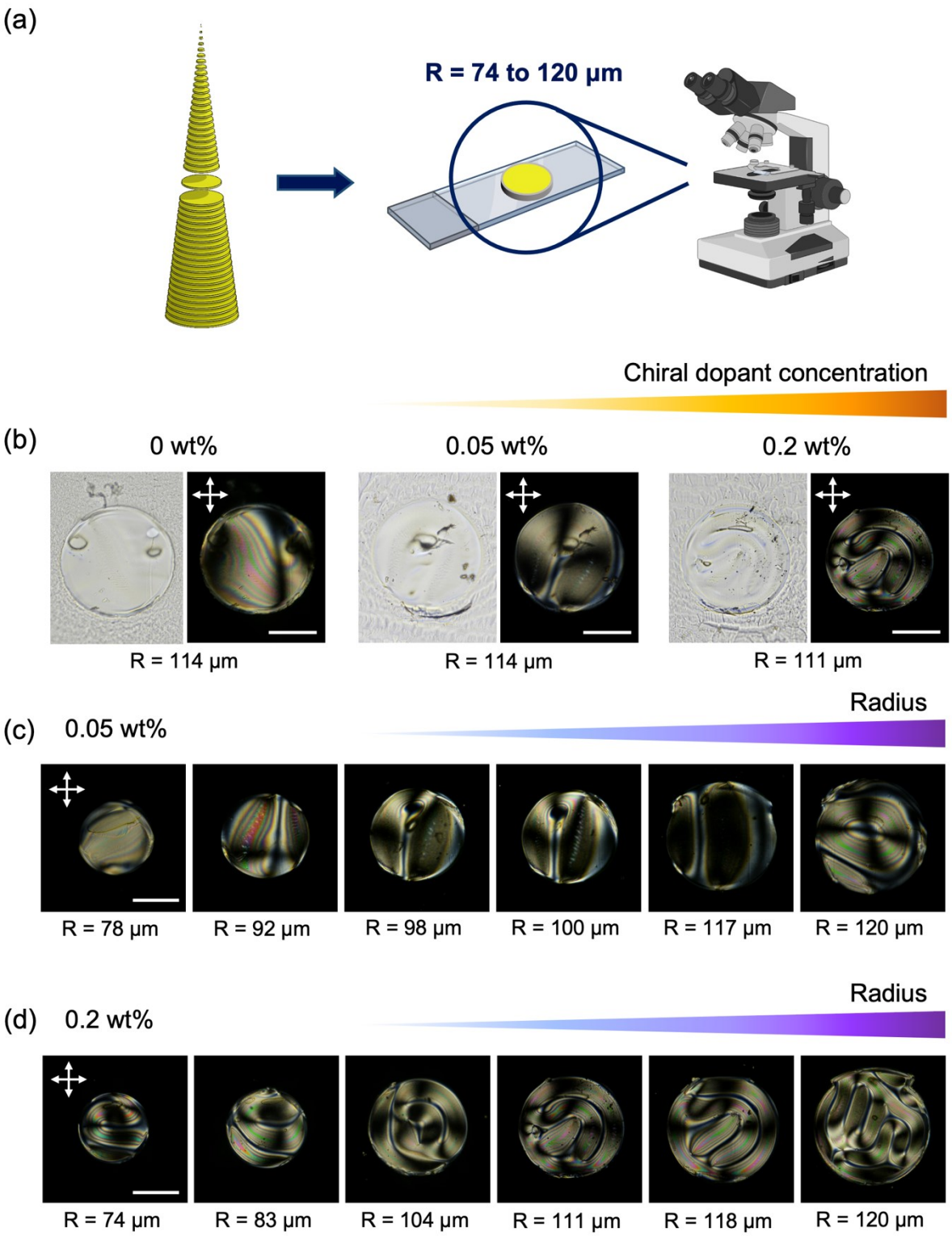

Figure 4. Molecular orientation in LCE microactuators depending on chiral dopant concentrations. a) Schematic of sectioning LCE microactuator and analyzing the cross-section under the polarized optical microscope (POM). b) Representative brightfield unpolarized and POM images of cross-sections of LCE microactuators with different chiral dopant concentrations (0, 0.05, and 0.2 wt%). Scale bar, 100 μm. c) Representative POM images of cross-sections of LCEs with 0.05 wt% of chiral dopant. Samples with smaller radius (R) are from closer to the needle tip. and d) LCEs with 0.2 wt% of chiral dopant. The cross-sections were obtained by slicing the microactuator along the short axis, commencing near the tip and

progressing toward the base (left to right). Scale bar, 100 μm. Arrows indicate the orientation of the analyzer and polarizer.

To understand the cause of the observed bending, an examination was performed on the region where bending was observed, characterized by a cross-sectional radius (R) ranging from 111 to 114 μm. Two distinct areas with different alignment were observed in LCE microactuators with 0.05 wt% of chiral dopant, which showed the largest bending angle. When observed between crossed polarizers, bright and dark regions (Figure 4b, see Figure S6a for the definition of the bright and dark region) can be identified. The bright region is hypothesized to largely have orientation in the plane of the section. This texture may be an intermediate state between a twisted bipolar structure (TBS) and a radial spherical structure (RSS) (also known as the spherulitic texture or the Frank-Pryce model). This intermediate state implies the helical rotation of molecules around the long axis of the microactuator.[45–48] We note that the intermediate state between TBS and RSS is found in tapered conical shaped LCE, which is reminiscent of texture in the spherical chiral nematic droplet.[45–48] In this microactuator, the precise director orientation within this domain is not critical, but we emphasize that the orientation is principally in the plane of the section.

The dark region in LCE with 0.05 wt% of chiral dopant indicates a domain with principally homeotropic alignment. The periphery of the section remains mostly dark when rotating the sample under crossed polarizers (Figure S6b and Movie S2). This suggests that the liquid crystal molecules are aligned along the long axis of the microactuator but may be slightly tilted. The combination of the relatively planar and homeotropic region explains the significant bending deformation in LCE. In the homeotropic regime, there is a contraction along the long axis of the actuator on heating (Figure S7). As the other side of the microactuator should exhibit a smaller expansion along the long axis of the microactuator, heating results in bending towards the homeotropic region.

This predictable, asymmetric director pattern was not observed in LCE with 0 and 0.2 wt% of chiral dopant (Figure 4b). At the same position of the microactuator, more symmetry in the director pattern was observed in LCE without chiral dopant. The lack of the predictable director pattern is consistent with the unpredictable deformation associated with this composition. In LCE loaded with 0.2 wt% of chiral dopant, only a fingerprint-like texture was observed. Consistent with the absence of significant bias in molecular orientation at this

position, bending in LCE with 0.2 wt% of chiral dopant only occurred at a position closer to the tip of the actuator (Figure 3a).

The chiral dopant concentration influences overall molecular orientation within the microactuator, which is not limited to the bending region alone. The molecular orientation along the length of LCE microactuators exhibited a noticeable difference depending on chiral dopant concentration. Moving from the tip toward the base of the microactuator, LCE with 0.05 wt% of chiral dopant showed the transition to an asymmetric texture characterized by the combination of the radial spherical texture and homeotropic domain (Figure 4c). In contrast, LCE with 0.2 wt% of chiral dopant exhibited the development of a fingerprint-like texture along the length of the actuator (Figure 4d).

2.5. Preferential bending direction determined by protrusion position

The fabrication process described is capable of producing a large number of LCE microactuators that bend in the same direction. Each feature of mold contains fractures. We hypothesized that this small fracture breaks the symmetry of the mold, influencing the bias in molecular orientation within the structure. The connection between the protrusion and shape changes of LCEs was studied by fabricating molds with fractures in different positions. Peeling the PDMS from the master mold in different directions produces fractures in different positions (**Figure 5**a). For example, the PDMS, which was peeled from north to south, experiences a fracture along the southern side of the cavities. The fractured shape gets transferred onto the LCEs, yielding them with the protrusion on the southern side of the actuators. Thus, we were able to produce four different PDMS molds. The prepared PDMS molds are denoted as PDMS-NS, PDMS-SN, PDMS-EW, and PDMS-WE, where the first letter represents from which direction the mold was peeled, and the second letter represents towards which direction it was peeled. Depending on the mold used, the LCE microactuators were named LCE-NS, LCE-SN, LCE-EW, and LCE-WE. The concentration of chiral dopant was set to 0.05 wt%.

The four types of LCE microactuator arrays exhibited prominent differences in molecular orientation. All four types of LCE microactuators showed both planar and homeotropic domains across the cross-section of the microactuator (Figure 5b). However, the position where the homeotropic domain lies within the structure is not the same. The cross-section of LCE-NS shows that the homeotropic region is positioned on the west side of the actuators,

whereas LCE-SN has the homeotropic region on the east side of them. For LCE-EW and LCE-WE, the homeotropic region was observed on the north and the south side of the actuators, respectively. These results suggest that a simple change in the position of protrusion makes liquid crystal molecules within confined structure align in different ways and varies the bias in molecular orientation. We note that for each type of actuators, we evaluated the bending direction across five different arrays.

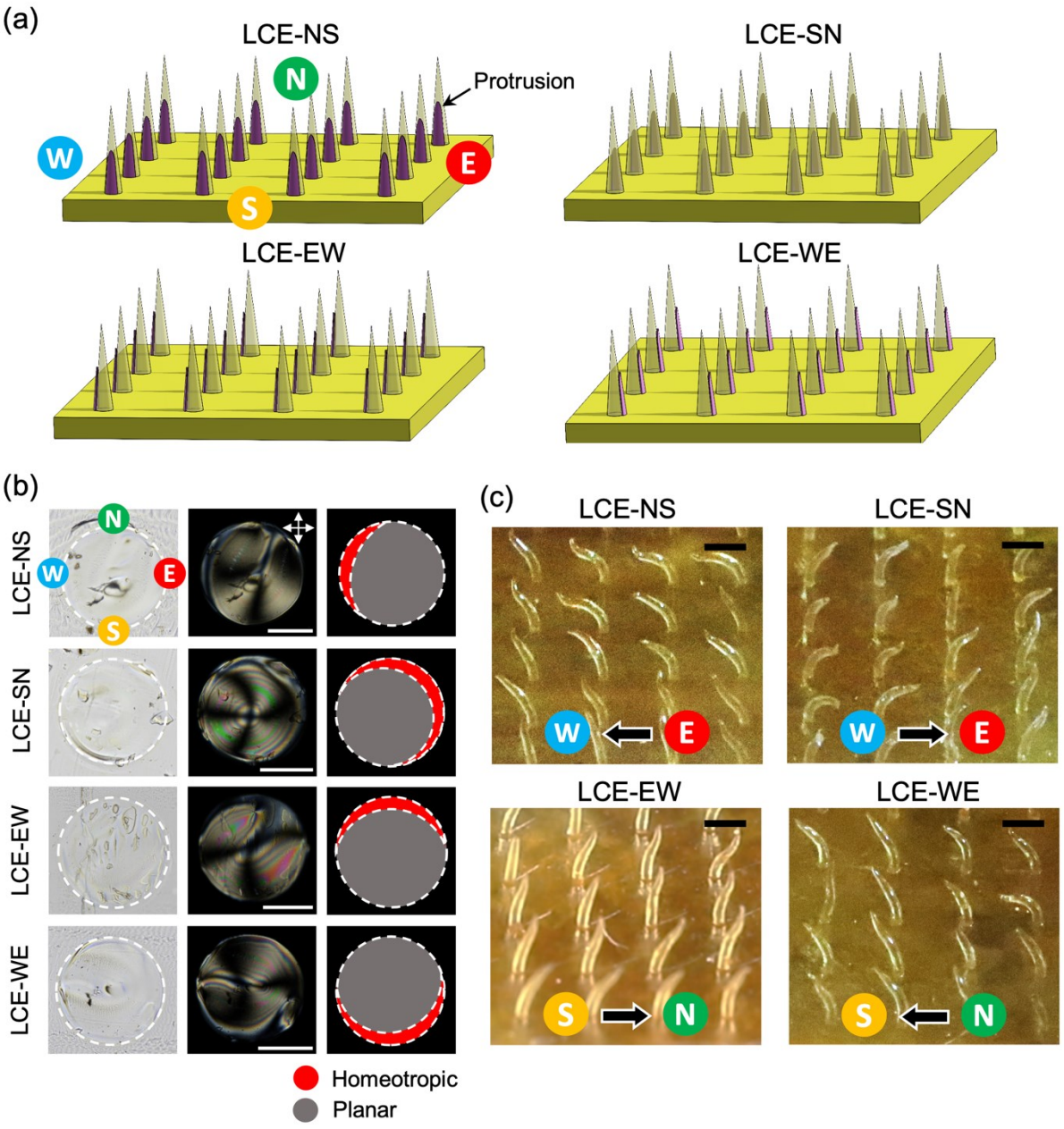

Figure 5. Controlling bending direction via programming protrusion position. a) Schematic of four types of LCE microactuator arrays with protrusion on different positions. The position of protrusion is specified using the four cardinal directions: North (N), East (E), South (S), and West (W). b) Representative brightfield unpolarized (first column) and POM images (second column) of cross-sections of LCE microactuators with different protrusion positions. The

third column shows schematic cross-sections of microactuators, which possess two domains with different molecular orientations. The molecular orientation was determined by POM images. The red and gray regions correspond to the relatively homeotropic and planar area, respectively. The white dashed line represents the circumference of sliced LCEs. Scale bar, 100 μm. c) Images of four types of LCE microactuator arrays bending in different directions when heated up to 180 °C. Scale bar, 1 mm. Arrows indicate the orientation of the analyzer and polarizer.

Controlling the bias in molecular orientation by protrusion positions, we fabricated LCE microactuator arrays that bend in various directions (Figure 5c). Upon heating 180 °C, LCE-NS microactuators bent from the east to the west side. The preferential bending direction is attributed to the homeotropic structure located on the west side of the actuators. In contrast, LCE-SN, where homeotropic alignment is observed on the east side, showed bending toward the east side of the actuators (Movie S3). Likewise, LCE-EW and LCE-WE showed bending deformation influenced by the protrusion positions and bias in molecular orientation. The accuracy of bending direction was measured by calculating a deviation angle from top view images of arrays (Figure S8a). A vector was drawn from each needle base to tip while heated. The deviation angle was measured as the angle between the actuator vector and the nominal bending direction. Positive angle indicates that actuator is deviating from the ideal bending direction in a clockwise direction, while a negative value was assigned for anticlockwise deviation. (Figure S8b).

Through the assembly of molds, LCEs with non-uniform bending actuation can be fabricated. Here, two types of molds were fabricated, PDMS-NS and PDMS-SN**.** Depending on how PDMS parts were assembled, the resultant LCEs exhibit different shape changes in response to heat. The first mold was assembled to produce LCE-NS in the west and LCE-SN in the east direction (**Figure 6**a). Upon heating, as microactuators in the west and the east bend toward the west and the east, respectively, the LCE microactuator arrays generate outward bending deformation. The second mold was prepared to have LCE-SN and LCE NS placed in the west and the east direction, respectively (Figure 6b). The resultant LCE microactuators showed inward bending deformation. The ease of fabricating complex molds and the wide range of assemblies that can be achieved make it feasible to develop arrays of LCE microactuators with diverse shape changes.

2.6. Preferential bending direction determined by handedness of chiral dopant

The handedness of the chiral dopant influences the spontaneous self-assembly of liquid crystal monomers within microsized molds. LCE microactuators were fabricated with chiral

dopant S811 with identical helical twisting power as R811 but opposite handedness. Consistent with previous results, relatively planar and homeotropic regions were observed in LCEs with 0.05 wt% of S811 (Figure S9). Interestingly, LCEs with S811 have the homeotropic region positioned in the opposite position compared to when R811 was added. For example, in LCE-NS with S811, homeotropic region was observed on the east side of actuators. In LCE-SN, homeotropic region was biased on the west side of actuators. For LCE-EW and LCE-WE, homeotropic region was observed on the south and north of actuators, respectively. As LCEs bend toward homeotropic region, bending of LCEs with S811 was observed in the opposite directions as compared to LCEs with R811. LCE-NS and LCE-SN showed bending toward the east and west, respectively. LCE-EW and LCE-WE bent toward homeotropic region as well, which is the south and north side of actuators.

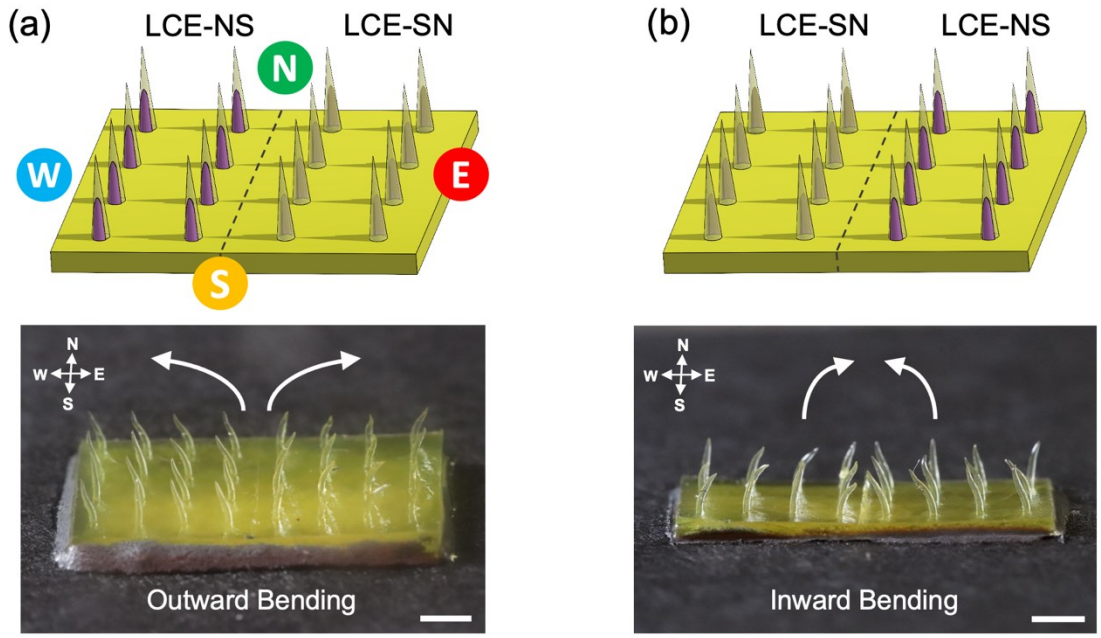

Figure 6. Complex bending of LCE microactuator arrays. a) Arrays of microactuators bending away from the center and b) toward the center at 180 °C. Scale bar, 2 mm.

3. Conclusion

Processing is key to develop stimuli-responsive structures with programmed shape changes at the microscale.[49-51] In this study, we describe a bottom-up fabrication strategy to create arrays of 3D LCE microactuators that undergo controlled and reversible bending deformations in response to heat. LCE microactuators were synthesized in needle-shaped micromolds, where liquid crystal molecules spontaneously self-assemble into ordered domains. Chiral dopant was introduced to induce the asymmetric molecular orientation within LCE

microactuators, generating large, reversible bending deformation when heated. The magnitude of bending was modulated by adjusting the concentration of chiral dopant and varying the chirality. The anisotropy of molecular orientation within the structure was programmed by controlling the protrusion positions on LCE microactuators or varying the handedness of chiral dopant. While surface alignment of liquid crystal monomers has largely been limited to two-dimensional structures[36] with a thickness of up to 100 μm,[52] we extended this method for producing three-dimensional molded structures with base width of 270 μm. We utilized the self-assembly of chiral nematic monomer solutions within confined space to yield spatially complex, controlled molecular alignment. We would like to highlight that our fabrication approach is a simple method which could enable mass production of microactuators.

We imagine these LCE microactuators to be utilized as thermally-responsive 'Velcro' which shows adhesion upon heating.[53] The ability to control bending in programmed, region-specific manner expands possibilities for applying these LCEs in microrobots,[34,35] microgrippers,[32,33] and microfluidic systems.[54] Formulating LCEs that are suitable for surface alignment and have lower transition temperatures would further improve the applicability of our microactuator system.

4. Experimental Section/Methods

Materials: The LC monomer, 1,4-bis-[4-(6-acryloyloxhexyloxy)benzoyloxy]-2-methylbenzene (RM82), was purchased from Wilshire Technologies, Inc. The amine chain extender, n-butylamine, was purchased from TCI America. The photoinitiator, Irgacure 369 (I-369), was purchased from Sigma-Aldrich. The chiral dopants, (R)-2-octyl 4-[4-(hexyloxy)benzoyloxy]benzoate (R811) and (S)-2-octyl 4-[4-(hexyloxy)benzoyloxy]benzoate (S811), were purchased from AmBeed. All materials were used as received.

Fabrication of PDMS mold: A commercial microneedle derma stamp (Dermastamp 140, Dermaroller System) was used as a master mold. The dimensions of the microneedles (MNs) on the stamp were a height of 2 mm, a base width of 270 μm, and a spacing between bases of 1807.4 ± 5.4 μm (n=2), with 140 needles in 17.5 mm x 25 mm area. The microneedle derma stamp was glued to the bottom of a plastic Petri dish with a diameter of 53 mm and a depth of

1.5 mm. A reverse mold was prepared by casting the PDMS precursor solution over the microneedle stamp. The PDMS (Sylgard 182, Dow Corning) mixture was prepared by mixing the base and curing agent in a weight ratio of 15:1. This PDMS elastomer was found to induce planar or titled orientation of the nematic monomer solution (Figure S10). After pouring, the master mold covered with the PDMS mixture was degassed in a desiccator under a vacuum to remove air bubbles and then cured at 70 °C for 2 h. The PDMS mold was peeled off from the master mold. The PDMS mold released from the master was further cured at 70 °C for 3 h.

Fabrication of LCE microactuators: The LC mixture was prepared by mixing RM82 and n-butylamine in 1.1:1 molar ratio with 1.5 wt% of I-369. The LC mixture was doped with varying concentrations of the chiral dopant R811 from 0 wt% to 0.2 wt%. As only a small amount of chiral dopant is required, a stock solution of chiral dopant was prepared by dissolving 1.9 mg of R811 per mL of acetone. The total solvent content in the monomer solution ranged from 0.25 µL/mg to 0.27 µL/mg. After heating and mixing, the mixture was poured onto the PDMS mold at 70 °C and then placed in an oven at 70 °C under a vacuum at -0.05 MPa for 15 h. Immediately after oligomerization, the sample was photopolymerized by the irradiation of 365 nm UV LED (LX400, OmniCure) for 15 min at room temperature with an intensity of 10 ± 1 mW cm^{-2}. Then, the partially cured sample was peeled off from the PDMS mold. After being removed from the mold, the sample was brought inside the UV chamber. The sample was flipped and then fully cured inside the UV chamber (UVP Crosslinker CL-3000, Analytik Jena) at 365 nm for 6 h with an intensity of 2.1 ± 0.07 mW cm^{-2}.

Characterization of actuation performance: To analyze shape change, LCE microactuators were cut off from the substrate with a razor blade. The LCE microactuator was placed on the glass slide with a droplet of silicone oil to prevent adhesion. The sample was placed on the thermal stage (LTS420, Linkam). Controlling the temperature of the thermal stage, the dimensional changes of the LCE microactuator were monitored via polarized optical microscope (Eclipse LV100N POL, Nikon) in transmission mode.

The bending angle was defined as the angle between the line connecting the center of the base and the tip at 30 °C and the line connecting the center of the base and the tip at an elevated temperature. The bending angle was measured using ImageJ analysis software.

The bending behavior of LCE microactuator arrays was analyzed by heating the entire structure on the hot plate. The base substrate was attached to the flat glass slide using the heat resistant epoxy adhesive (HighHeat^{TM}, J-B Weld). The entire LCE microactuator was then placed on the hot plate, and the shape change was observed from 30 to 180 °C. To ensure uniform heating, the experiments were done inside a glass container surrounding the sample. The shape change of LCE microactuator was monitored with a digital single-lens reflex camera (EOS Rebel T7i, Canon).

Characterization of morphology: The resin block was prepared by embedding a single LCE microactuator in epoxy resin. To avoid the increase in temperature by the exothermic curing, the epoxy resin and curing agent (EpoxiCure 2, Buehler) with low heat of reaction was used. The epoxy mixture was prepared by mixing the resin and hardener in a volume ratio of 4:1 and then cured overnight at room temperature. The resin blocks prepared were sliced into thin sections using a microtome (Leica UC7 Ultramicrotome, Leica Microsystems) with a glass knife at room temperature.

The cross sections were placed on microscope slides with silicone oil and inspected using POM equipped with the thermal stage. To erase the material deformation induced by the sectioning, the sample was first heated up to 180 °C and then cooled back to room temperature. Subsequently, the morphology of cross sections at room temperature and their transition in response to temperature were analyzed with parallel and crossed polarizers.

Analysis of surface morphology: The surface morphology of LCE microactuator arrays was analyzed by Scanning Electron Microscopy (SEM) (Tescan Vega, Tescan). The LCE microactuator arrays were sputter coated with gold using a sputter coater (108 Sputter Coater, Cressington Scientific Instruments). The sample was placed inside the SEM chamber and imaged at various tilt angles.

Statistical Analysis: Outliers were excluded based on Cook's distance (One from LCEs with 0.1 and 0.2 wt% of chiral dopant, respectively). The normal distribution of data samples was verified using the Shapiro-Wilk test, and differences between groups of samples were tested using one-way analysis of variance (ANOVA) followed by Dunnett's multiple comparisons test. A significance level of 0.05 was used, and $p<0.05$ was used to indicate statistical

significance. Bin width of the histogram is chosen to be 20˚. The statistical analysis was done using the software GraphPad Prism 9.

Supporting Information

Supporting Information is available from the Wiley Online Library.

Acknowledgements

This work was supported by the National Science Foundation under Grant No. DMR 2041671. The authors would like to thank Sungee Hong (Texas A&M University) for helpful discussions. The authors also would like to acknowledge the use of the Microscopy and Imaging Center at Texas A&M University. Schematic was created with Biorender (https://biorender.com/)

Conflict of Interest

The authors declare no conflict of interest.

Data Availability Statement

The data that support the findings of this study are available from the corresponding author upon reasonable request.

Received: ((will be filled in by the editorial staff))
Revised: ((will be filled in by the editorial staff))
Published online: ((will be filled in by the editorial staff))

References

[1] A. Dolev, M. Kaynak, M. S. Sakar, *Adv. Intell. Syst.* **2021**, *3*, 2000233.

[2] M. Wei, Y. Gao, X. Li, M. J. Serpe, *Polym. Chem.* **2017**, *8*, 127.

[3] S. Palagi, P. Fischer, *Nat. Rev. Mater.* **2018**, *3*, 113.

[4] C.-Y. Lo, Y. Zhao, Y. Ma, S. Wu, Y. Alsaid, M. M. Peet, R. E. Fisher, H. Marvi, D. M. Aukes, S. Berman, X. He, Springer International Publishing, Cham, **2021**.

[5] Y. Zuo, L. Zheng, C. Zhao, H. Liu, *Small* **2020**, *16*, 1903849.

[6] H. Ding, Q. Zhang, H. Gu, X. Liu, L. Sun, M. Gu, Z. Gu, *Adv. Funct. Mater.* **2020**, *30*, 1901760.

[7] M. Hippler, E. Blasco, J. Qu, M. Tanaka, C. Barner-Kowollik, M. Wegener, M. Bastmeyer, *Nat. Commun.* **2019**, *10*, 232.

[8] A. Ennis, D. Nicdao, S. Kolagatla, L. Dowling, Y. Tskhe, A. J. Thompson, D. Trimble, C. Delaney, L. Florea, *Adv. Funct. Mater.* **2023**, 2213947.

[9] X. Liu, M. Gao, J. Chen, S. Guo, W. Zhu, L. Bai, W. Zhai, H. Du, H. Wu, C. Yan, Y. Shi, J. Gu, H. J. Qi, K. Zhou, *Adv. Funct. Mater.* **2022**, *32*, 2203323.

[10] Y. Liang, W. Cui, L. Li, Z. Yu, W. Peng, T. Xu, *Adv. Opt. Mater.* **2019**, *7*, 1801269.

[11] X. Fu, J. Cai, X. Zhang, W.-D. Li, H. Ge, Y. Hu, *Adv. Drug Deliv. Rev.* **2018**, *132*, 169.

[12] A. Biswas, I. S. Bayer, A. S. Biris, T. Wang, E. Dervishi, F. Faupel, *Adv. Colloid Interface Sci.* **2012**, *170*, 2.

[13] J. E. Park, S. Won, W. Cho, J. G. Kim, S. Jhang, J. G. Lee, J. J. Wie, *J. Polym. Sci.* **2021**, *59*, 1491.

[14] K. Ni, Z. Wang, *Adv. Funct. Mater.* **2023**, 2213350.

[15] C. L. van Oosten, C. W. M. Bastiaansen, D. J. Broer, *Nat. Mater.* **2009**, *8*, 677.

[16] M. Warner, E. M. Terentjev, *Liquid Crystal Elastomers*, Oxford University Press, Oxford **2007**.

[17] K. M. Herbert, H. E. Fowler, J. M. McCracken, K. R. Schlafmann, J. A. Koch, T. J. White, *Nat. Rev. Mater.* **2022**, *7*, 23.

[18] T. J. White, D. J. Broer, *Nat. Mater.* **2015**, *14*, 1087.

[19] R. S. Kularatne, H. Kim, J. M. Boothby, T. H. Ware, *J. Polym. Sci., Part B: Polym. Phys.* **2017**, *55*, 395.

[20] C. Ohm, M. Brehmer, R. Zentel, *Adv. Mater.* **2010**, *22*, 3366.

[21] Z. Wang, H. Tian, Q. He, S. Cai, *ACS Appl. Mater. Interfaces* **2017**, *9*, 33119.

[22] N. Torras, K. E. Zinoviev, J. Esteve, A. Sánchez-Ferrer, *J. Mater. Chem. C.* **2013**, *1*, 5183.

[23] J. Lee, Y. Guo, Y.-J. Choi, S. Jung, D. Seol, S. Choi, J.-H. Kim, Y. Kim, K.-U. Jeong, S. Ahn, *Soft Matter* **2020**, *16*, 2695.

[24] S. Li, M. M. Lerch, J. T. Waters, B. Deng, R. S. Martens, Y. Yao, D. Y. Kim, K. Bertoldi, A. Grinthal, A. C. Balazs, J. Aizenberg, *Nature* **2022**, *605*, 76.

[25] A. Buguin, M.-H. Li, P. Silberzan, B. Ladoux, P. Keller, *J. Am. Chem. Soc.* **2006**, *128*, 1088.

[2*6*] Y. Yao, J. T. Waters, A. V. Shneidman, J. Cui, X. Wang, N. K. Mandsberg, S. Li, A. C. Balazs, J. Aizenberg, *Proc. Natl. Acad. Sci. USA* **2018**, *115*, 12950.

[27] S. Schuhladen, F. Preller, R. Rix, S. Petsch, R. Zentel, H. Zappe, *Adv. Mater.* **2014**, *26*, 7247.

[28] J. T. Waters, S. Li, Y. Yao, M. M. Lerch, M. Aizenberg, J. Aizenberg, A. C. Balazs, *Sci. Adv.* **2020**, *6*, eaay5349.

[29] C. Ohm, C. Serra, R. Zentel, *Adv. Mater.* **2009**, *21*, 4859.

[30] C. Ohm, N. Kapernaum, D. Nonnenmacher, F. Giesselmann, C. Serra, R. Zentel, *J. Am. Chem. Soc.* **2011**, *133*, 5305.

[31] V. S. R. Jampani, R. H. Volpe, K. R. de Sousa, J. F. Machado, C. M. Yakacki, J. P. F. Lagerwall, *Sci. Adv.* **2019**, *5*, eaaw2476.

[32] J. C. Breger, C. Yoon, R. Xiao, H. R. Kwag, M. O. Wang, J. P. Fisher, T. D. Nguyen, D. H. Gracias, *ACS Appl. Mater. Interfaces* **2015**, *7*, 3398.

[33] Q. Ge, A. H. Sakhaei, H. Lee, C. K. Dunn, N. X. Fang, M. L. Dunn, *Sci. Rep.* **2016**, *6*, 31110.

[34] M. Wehner, R. L. Truby, D. J. Fitzgerald, B. Mosadegh, G. M. Whitesides, J. A. Lewis, R. J. Wood, *Nature* **2016**, *536*, 451.

[35] T. Xu, J. Zhang, M. Salehizadeh, O. Onaizah, E. Diller, *Sci. Robot.* **2019**, *4*, eaav4494.

[36] T. H. Ware, M. E. McConney, J. J. Wie, V. P. Tondiglia, T. J. White, *Science* **2015**, *347*, 982.

[37] Y. Shiine, H. Nishikawa, Y. Furuta, K. Kanamitsu, T. Satoh, Y. Ishii, T. Kamiya, R. Nakao, S. Uchida, *Microelectron. Eng.* **2010**, *87*, 835.

[38] S. Wang, D. Feng, C. Hu, P. Rezai, *J. Semicond.* **2018**, *39*, 086001.

[39] A. Ghatak, M. K. Chaudhury, *Langmuir* **2003**, *19*, 2621.

[40] C. Kim, M.-A. Yoon, B. Jang, H.-D. Kim, J.-H. Kim, A. T. Hoang, J.-H. Ahn, H.-J. Jung, H.-J. Lee, K.-S. Kim, *NPG Asia Mater.* **2021**, *13*, 44.

[41] W. W. Tooley, S. Feghhi, S. J. Han, J. Wang, N. J. Sniadecki, *J. Micromech. Microeng.* **2011**, *21*, 054013.

[42] S.-W. Ko, S.-H. Huang, A. Y.-G. Fuh, T.-H. Lin, *Opt. Express* **2009**, *17*, 15926.

[43] H. Nemati, D.-K. Yang, K.-L. Cheng, C.-C. Liang, J.-W. Shiu, C.-C. Tsai, R. S. Zola, *J. Appl. Phys.* **2012**, *112*, 124513

[44] Y. Xia, E. Lee, H. Hu, M. A. Gharbi, D. A. Beller, E.-K. Fleischmann, R. D. Kamien, R. Zentel, S. Yang, *ACS Appl. Mater. Interfaces* **2016**, *8*, 12466.

[45] Y. Zhou, E. Bukusoglu, J. A. Martínez-González, M. Rahimi, T. F. Roberts, R. Zhang, X. Wang, N. L. Abbott, J. J. de Pablo, *ACS Nano* **2016**, *10*, 6484.

[46] E. Bukusoglu, X. Wang, Y. Zhou, J. A. Martínez-González, M. Rahimi, Q. Wang, J. J. de Pablo, N. L. Abbott, *Soft Matter* **2016**, *12*, 8781.

[47] F. Xu, P. P. Crooker, Phys. Rev. E **1997**, *56*, 6853.

[48] D. Seč, T. Porenta, M. Ravnik, S. Žumer, *Soft Matter* **2012**, *8*, 11982.

[49] H. Zeng, D. Martella, P. Wasylczyk, G. Cerretti, J. G. Lavocat, C. Ho, C. Parmeggiani, D. S. Wiersma, *Adv. Mater.* **2014**, *26*, 2319.

[50] H. Zeng, P. Wasylczyk, C. Parmeggiani, D. Martella, M. Burresi, D. S. Wiersma, *Adv. Mater.* **2015**, *27*, 3883.

[51] A. Bunea, D. Martella, S. Nocentini, C. Parmeggiani, R. Taboryski, D. S. Wiersma, *Adv. Intell. Syst.* **2021**, *3*, 2000256.

[52] J. Boothby, T. H. Ware, *Soft Matter* **2017**, *13*, 4349.

[53] S. Y. Yang, E. D. O'Cearbhaill, G. C. Sisk, K. M. Park, W. K. Cho, M. Villiger, B. E. Bouma, B. Pomahac, J. M. Karp, *Nat. Commun.* **2013**, *4*, 1702.

[54] X. Dong, G. Z. Lum, W. Hu, R. Zhang, Z. Ren, P. R. Onck, M. Sitti, *Sci. Adv.* **2020**, *6*, eabc9323.